Numerical Modeling of the Alumina Distribution in Aluar Cells

Dagoberto S. Severo[1], Vanderlei Gusberti[2], Pablo Navarro[3] and Marcos Domínguez[4]
1. Director
2. PhD Engineer
CAETE Engenharia Ltda, Porto Alegre, RS, Brazil
3. Head of Electrochemical Process R&D
4. Process Analyst
Aluar Aluminio Argentino SAIC, Puerto Madryn, Argentina
Corresponding author: dagoberto@caetebr.com

Abstract

This article presents the use of numerical modelling of the alumina transport and distribution in Aluar's end-to-end end-risers cells. The numerical models were built based on the MHD behavior of the cell, which includes the metal heave and the bubble flow evolving from the anodes. The anode slots were modelled at different times over the anode rota, producing a 3D bath flow solution for each timeframe situation. The influence of different aspects of alumina transport mechanism in the bath was studied separately in the models, such as metal drag at the interface, internal bath MHD forces and bubble induced forces. The model was validated with bath temperature measurements over time and showed a good agreement with the experimental findings.

The models were useful to analyze the alumina distribution pattern with the current configuration of point feeding locations enabling the virtual test of improvements by modifying the feeder location and feeding strategies. It was also possible to identify areas of bath stagnation in the bath volume, which can be associated with practical observations regarding carbon dust and
undissolved alumina.
The model predicted the anode position that systematically shows a tendency to operate with lower alumina concentration and which is prone to start an anode effect. Configurations that show a better alumina distribution and which should result in better process efficiency than the existing feeding procedure were obtained.

Keywords: alumina distribution, feeder location, anode effect, current efficiency, alumina transport.

1. Introduction

In aluminium electrolysis smelters, there is always pressure on better energy efficiency associated with production increase. In this context, some actions are frequently adopted such as: anode area increasing, ACD lowering and line current increasing. Those modifications reduce the bath volume of the cell and further increase the alumina dissolution capacity demand. The ability of the bath to dissolve alumina is therefore a critical aspect in cell design development. In addition to the sufficient bath volume, other conditions are important to promote good alumina dissolution such as superheat, alumina dump size and frequency, bath flow and turbulence.

Another relevant aspect is the alumina transport from the feeding locations to the ACD regions below each anode, where the electrolysis reactions occur. It is desirable that the convective transport ensures concentration homogeneity among all anodes. If one of the anodes is not

adequately served with alumina rich bath, it will become prone to produce successive anode effects during cell operation, reducing cell electrolysis efficiency.

The objective of this work is to develop numerical models capable of studying the alumina transport behavior inside the bath. Using the models, it is possible to study alternative feeding strategies in order to find a configuration that optimizes alumina distribution inside the bath, which is beneficial to increase electrolysis efficiency. Experimental work was carried out at ALUAR and it helped to develop and calibrate the numerical models.

Back in 2007, CAETE Engenharia developed bath flow models [1] where the bubble induced forces and MHD forces were included in the model formulation. The efficiency of the use of anode slots was the focus of the referred work. It was then concluded that the gas bubbles are the major contributor for the bath flow. However, the inclusion of MHD forces and metal drag is important to represent the asymmetry present in the bath flow of the cell. In [5] and [6], the bath flow results and alumina concentration are symmetric because no MHD effect is included in the simulation.

The same conclusions were made by another work about the importance of the bubble induced flow on the alumina transport by the bath [2], in opposition to some alumina distribution models also present in the literature [3, 4]. Alumina distribution in the bath space was measured by Tessier et al. [7]. Important variation on the concentration of alumina over the space and time was found and the bath flow pattern is responsible for the alumina dissolution and distribution in the electrolyte. They reported that “sick pots” presented stronger alumina concentration variation.

One possible experimental way to track alumina transport is measuring the bath temperature over time at selected channel positions. Usually, after the feeding shot, a transient drop in the bath temperature is observed along the alumina transport path in the bath, because fresh alumina is entering the bath at ambient temperature and energy is consumed to heat up and to dissolve the alumina. The sensor must be located at the downstream of the feeding position regarding the bath flow pattern. The temperature drop means that alumina rich bath is passing at the sensor area at the moment. After a certain time, the bulk hot bath comes back to the sensor region ending the temperature perturbation. As alumina heats up and dissolves, this effect fades and the particular bath temperature disturbance is not detectable anymore, this occurs far from the feeding positions or upstream to the feeders. In this work, as described above, the temperature measurement of the bath at selected positions will be used to infer the alumina concentration variation in time and space during the electrolysis process. Other processes can cause bath temperature variation such as non-uniformities in bath energy generation and consumption, heat losses through the holes, anode spike, etc. However, the type of temporal temperature variation of alumina feeding is very distinguishable because it matches with feeder frequency. Also, the magnitude and rate of the variation is usually higher compared to the other cited phenomena.

2. Bath Flow - Model Description and Assumptions

The fluid flow models were developed using the Finite Volume Method. The space occupied by the bath is the discretized geometry. The model physics is described as Euler-Euler multiphase flow with one continuous phase (liquid bath) and one dispersed phase (bubbles). Turbulence models are included in both fluid phases: k-epsilon model for bath and Zero-equation model for the bubbles.

The dominant electrolysis reaction of the process produces metallic Al and CO_2:

$$2Al_2O_3 + 3C = 4Al + 3CO_2 \quad (1)$$

The amount of gas generated obeys the Faraday's laws of electrolysis, for a given cell current and current efficiency.

The gas movement near the anode surface will induce the bath movement. Additionally, the MHD forces inside the bath volume and the metal drag forces are also included in the model. The MHD forces and interface velocities were obtained from earlier MHD models developed for ALUAR.
The top liquid surface allows the gas flow through the boundary. The model geometry includes the metal-bath interface deformation "dome-shaped" as obtained by MHD models (see example in Figure 1). As a matter of simplification, we consider that CO_2 is totally generated by the anode horizontal surface facing anode-cathode distance (ACD) (no lateral generation).

The bath density was estimated to 2070 kg/m^3. The value used for viscosity is: 0.0033 Pas. Figure 1 shows the metal-bath interface deformation applied to the bath volume geometry.

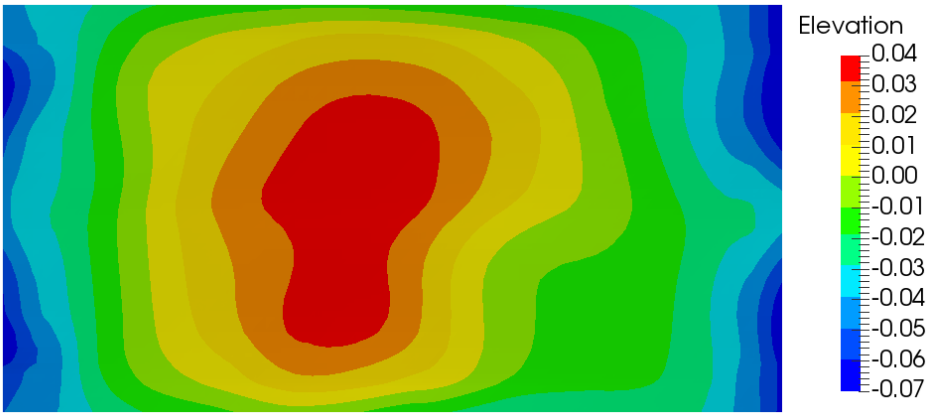

Figure 1. Metal-bath interface deformation applied to the model (m).

3. Alumina Transport - Model Description and Assumptions

Once the bath and gas flow velocities are obtained, the alumina transport inside the bath can be evaluated by inserting a scalar variable (tracer). We adopted the following model assumptions:

- Averaged steady state approach;
- Cell bath starts at 3.5 % homogeneous alumina concentration;
- It is assumed that kinematic diffusivity of the alumina is negligible compared with the advective transport produced by bath velocities;
- Alumina is continuously fed and consumed at constant rate (stoichiometric) until convergence is achieved. Alumina input: at 4 feeding positions. Alumina output: anode surface facing ACD;
- A final averaged alumina concentration field is achieved, homogeneous field means good mixing. The estimated time averaged concentration at ACD under each anode is calculated. Uniformity between all anodes is desirable.

It is also important to list some model limitations, reminding that the conclusions of this study must be interpreted accordingly.

- The model cannot track non-dissolved alumina meaning that there is no sludge in the model;

- The steady state approach does not differentiate the shot mass and time intervals as well as no under- and overfeeding sequences. To study these parameters, a fully transient model must be employed, which is computationally heavier.

In order to illustrate the outcome of this methodology, the Figure 2 shows the final time averaged alumina distribution for the existing feeding situation using the no slots anode geometry.

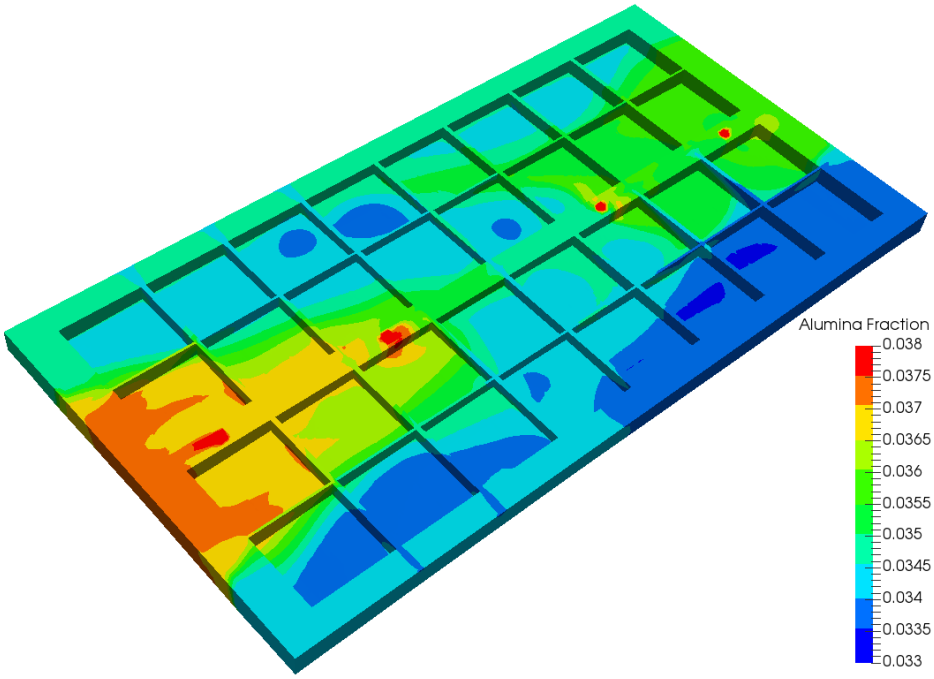

Figure 2. Alumina concentration field, time averaged.

For this case higher alumina concentrations are found near the endwalls of the cell, while the lowest concentrations are found near the sidewalls.

4. Validation - Temperature Measurements X Alumina Concentration Model

The bath temperature variation after a feeding shot gives indication of the presence or absence of fresh alumina at the measured position. ALUAR conducted some bath temperature measurements at points C1 to C14 shown in Figure 3, investigating the fate of the alumina fed by each one of the feeders (F1, F2, F3 and F4 in Figure 3). The experiment consisted in 4 sequential phases: in each phase only 1 feeder was activated during 10 minutes (approximately 10 shots), starting from upstream (F1 and F2) to downstream (F3 and F4). A special transient model was developed in order to reproduce the same experiment in a virtual numerical model.

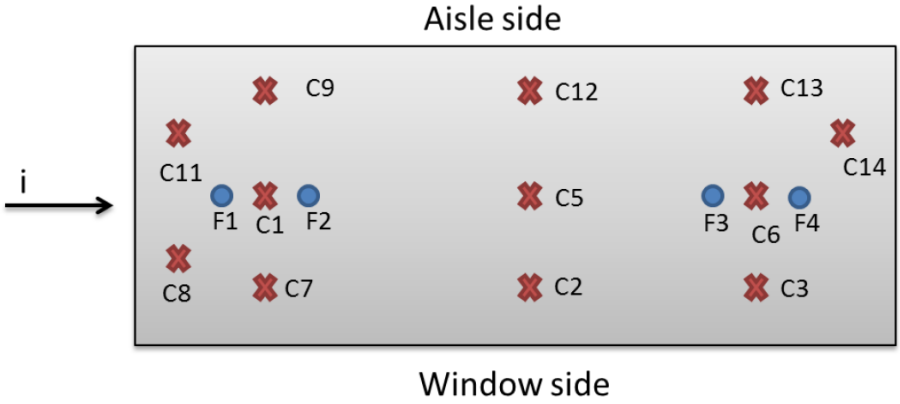

Figure 3. Feeder positions (F) and measured locations (C).

From the data some observations were made. Measured temperatures at upstream side of the cell showed good correlation with alumina feeding shots when feeders F1 and F2 were acting, mainly at C8 and C11, see Figure 4.

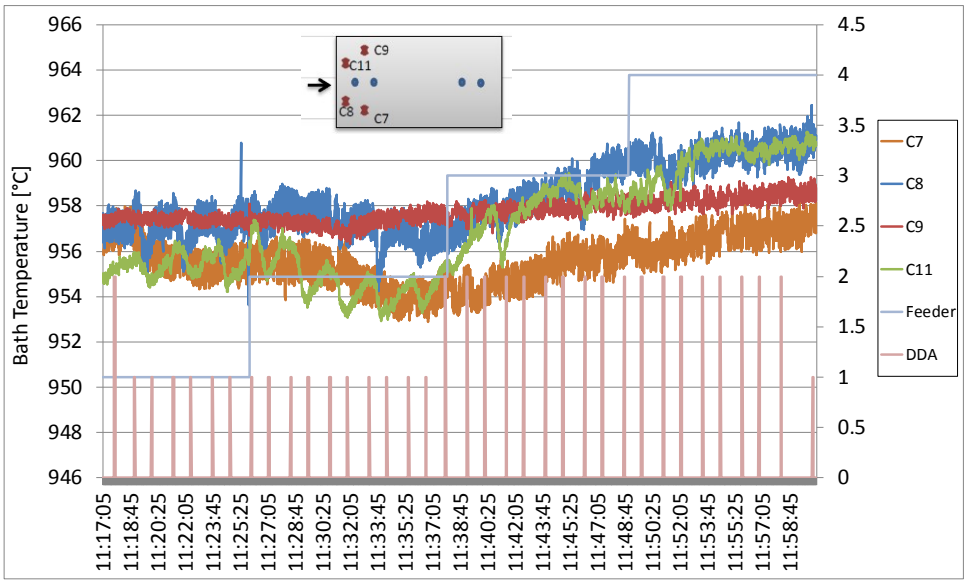

Figure 4. Measured bath temperature at upstream side during the test.

At the downstream side, the correlation between temperature measurements and feeding shots is not observed as it would be expected by symmetry (Figure 5), the behavior of C6 should be similar to C1 when F3 or F4 is acting. The explanation of such behavior in measurements is yet to be explained.

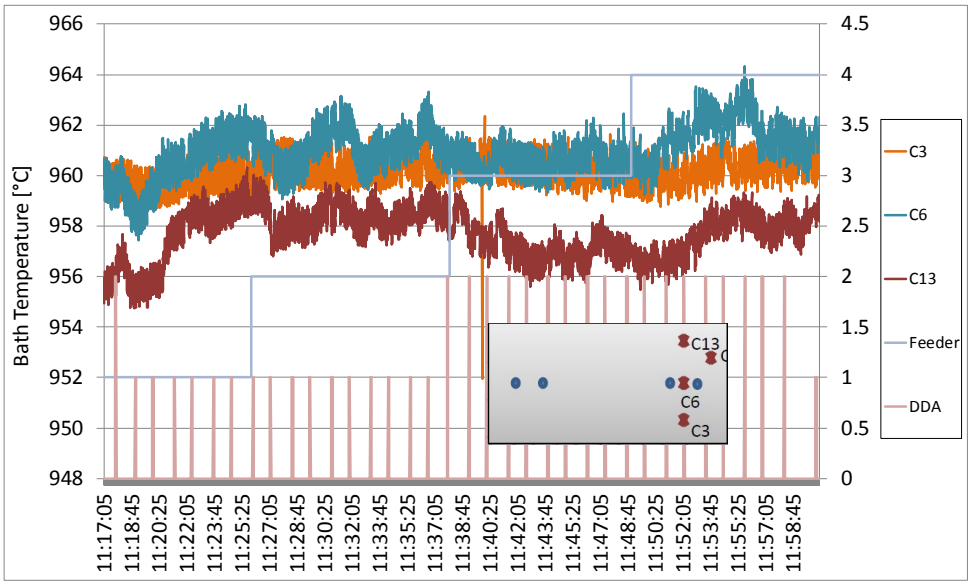

Figure 5. Measured bath temperature at downstream side during the test.

The numerical transient model developed to reproduce the measurements assumes that each feeder dumps 10 shots in intervals of 60 seconds, performing a total of 40 in 40 minutes. The anode slots geometry is included with the same configuration given by anode ages during the experiment. The alumina concentration was monitored at the same positions where the temperature was measured in the experiment.

For each feeder, a particular set of positions presents more sensibility, for example, point C1 presented more variations when F2 was active. In several points, good correlation between bath temperature and calculated alumina concentration was found as shown, for example, in Figure 6 and Figure 7. The temperature is expected to be lower in regions of high alumina concentrations.

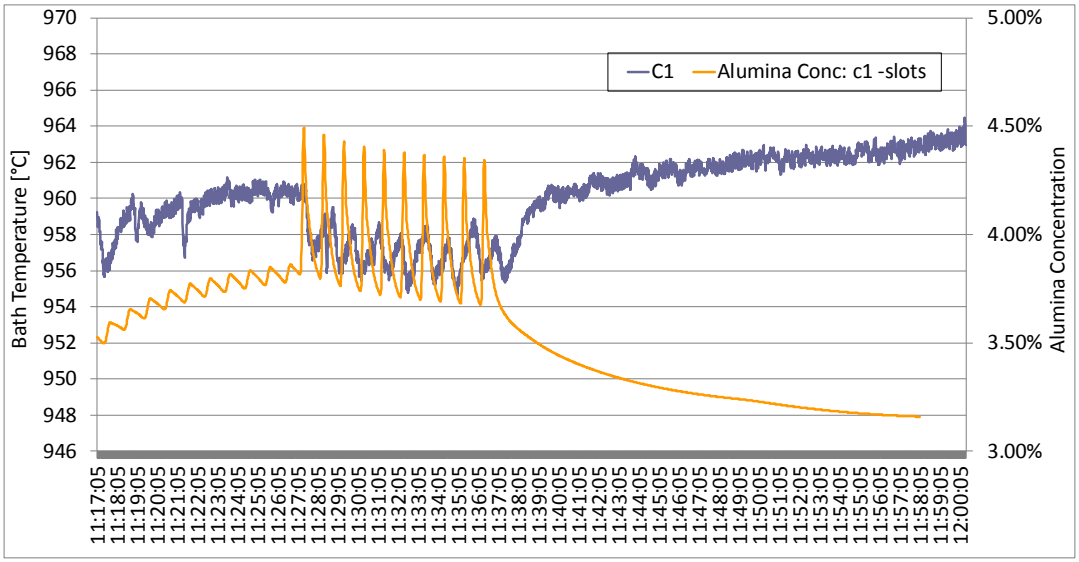

Figure 6. Measured bath temperature versus calculated alumina concentration for C1.

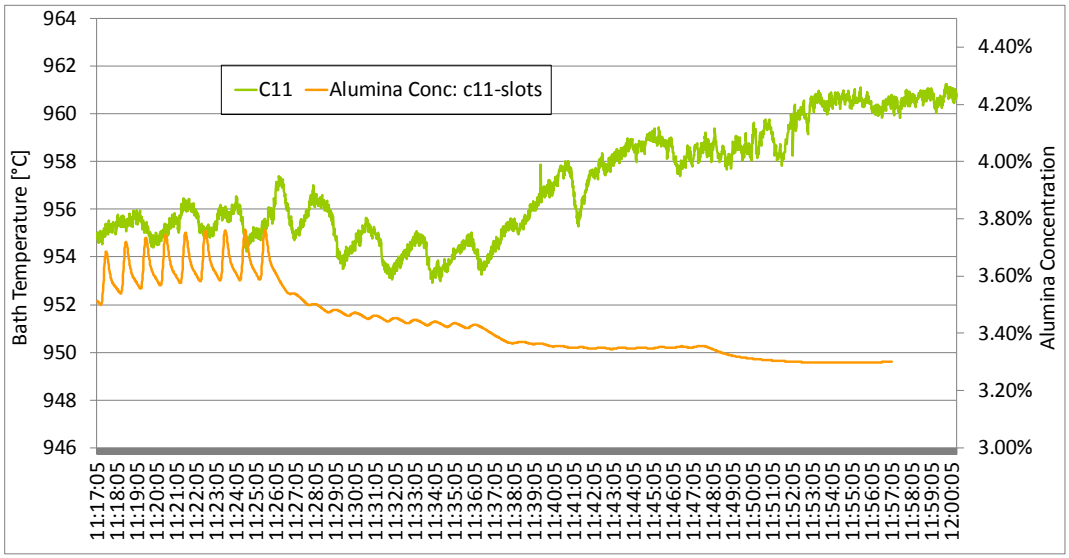

Figure 7. Measured bath temperature versus calculated alumina concentration for C11.

The transport of alumina has been successfully implemented in the model and agrees with the observations obtained from experimental work. In general, the correlations are very good at the points where the sensibility to alumina feeding was detected by the experiment. At some other points, because the measurements showed inconsistent temperature response, the comparisons were meaningless and they will not be reproduced in this work. One hypothesis why downstream measurements locations presented no sensibility to the experiment may be that the alumina dump is not passing through the exact position of the thermocouple. Another hypothesis may be the timeframe of shots at F3 and F4. Those feeders started to work after F1 and F2. At that moment, there might be enough time for the thermocouples installed at downstream (C3, C6, C13, C14) to have formed a solidified bath layer on the sensor, reducing sensibility to bath temperature.

5. Description of Proposed Feeding Cases

Some alternatives regarding the feeders' position and number were proposed. The new options also include modifications on tapping position, (A3 or A4) that may result in different bath flow patterns. All the cases are described in Table 1. The Figure 8 describes the position of the feeders in a top view of the cell.

Table 1. Description of tested feeder arrangements.

	Tapping Position	Number of feeders	Position
Case 1	Existing	4	Existing position (anodes 1-3-6-8)
Case 2	Anode A4	4	Existing position (anodes 1-3-6-8)
Case 3	Existing	4	Feeders at inter-anode channels, 1/2-3/4-5/6-7/8
Case 4	Anode A3	3	Feeders at anodes 2-4/5-7 position
Case 5	Anode A3	3	Feeders at anodes 1/2-4/5-7/8 position
Case 6	Anode A3	3	Feeders at anodes 1/2-4/5-7/8 position, middle feeder with double shot mass

In the Figure 8, the circles mark the feeding positions; a bigger circle means that more alumina is fed at that position than other locations. The direction of electric current is upstream at the left side, downstream at the right side.

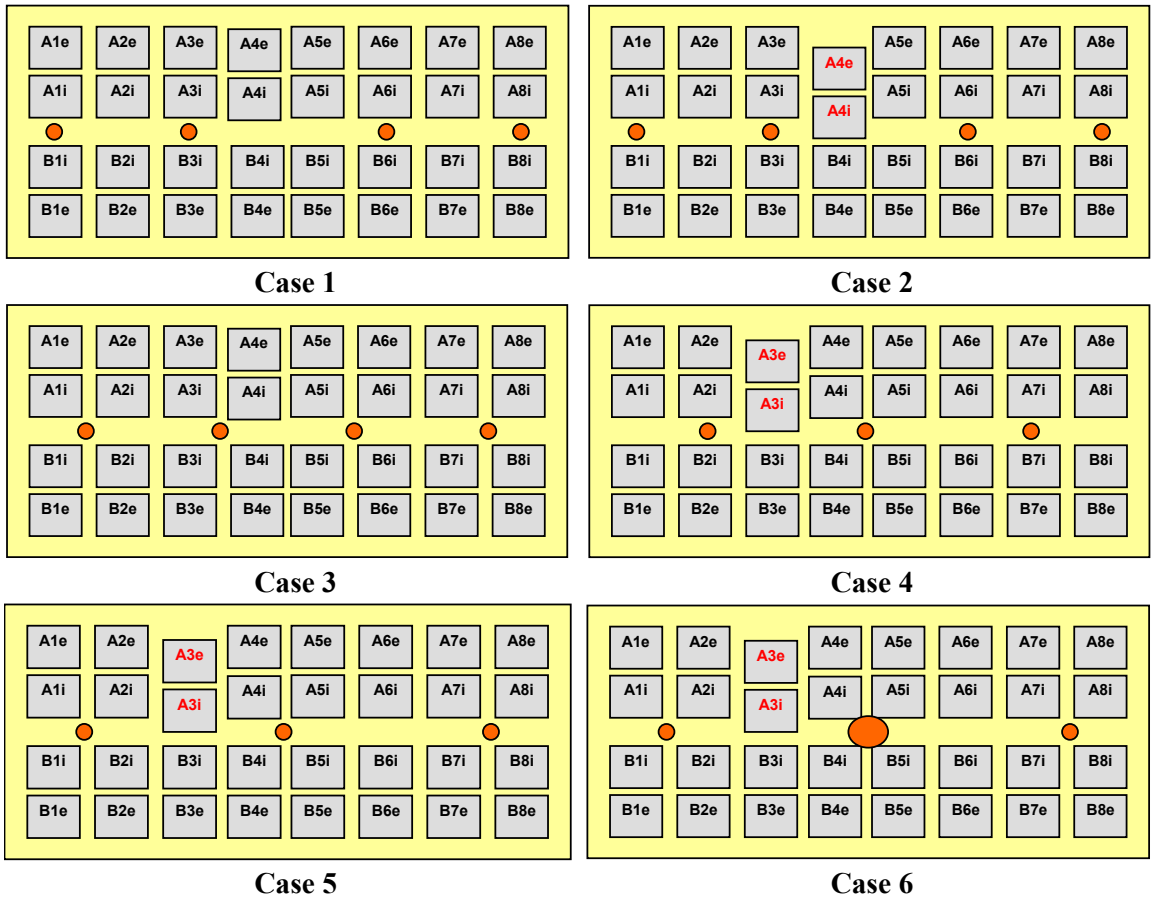

Figure 8. Feeder positions and anode configuration for the calculated cases.

The aluminium tapping is currently done at the sidewall between anodes. There is the intention to change the tapping procedure to be done at the middle of one anode position (A3 or A4). This requires the anode to be displaced towards the central channel to open space at the side channel for tapping. Numerical simulations of the tapping position at anodes A3 and A4 are used to study the alumina transport in the bath.

6. Results of Proposed Studies

6.1 Alumina Concentration in the Bath for Feeding Cases

For each one of the feeding cases of Table 1, 16 bath flow models and 16 alumina concentration simulations were performed. Each simulation adopts a different anode change configuration in order to reproduce the anode slot pattern present at the moment that is dependent on anode life in the cell.

Each slot configuration modifies the bath flow and alumina transport pattern. The following pictures (Figure 9 to Figure 14) show the alumina concentration field for each feeding case, after the anode change A1. Similar results were obtained for the other 15 anode changes which are not presented in this work.

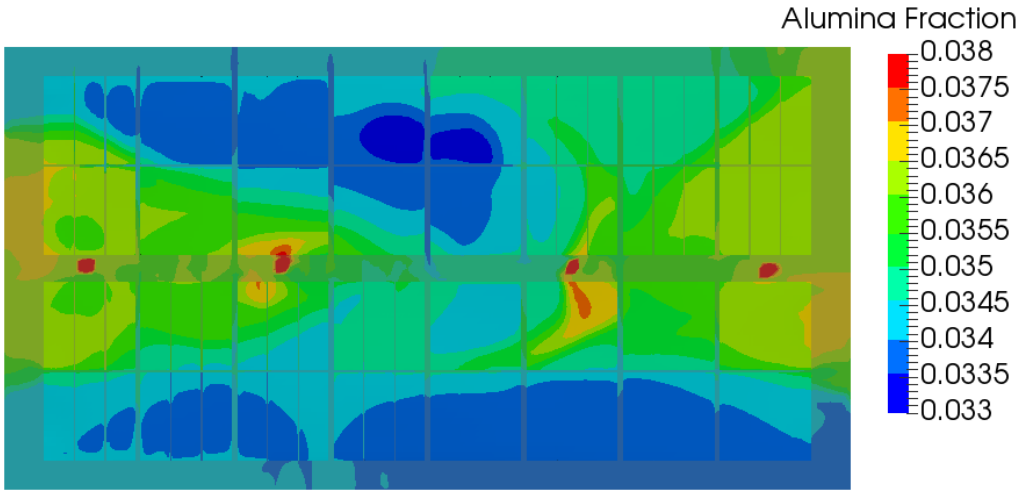

Figure 9. Alumina concentration in the bath volume after anode A1 is changed, Case 1.

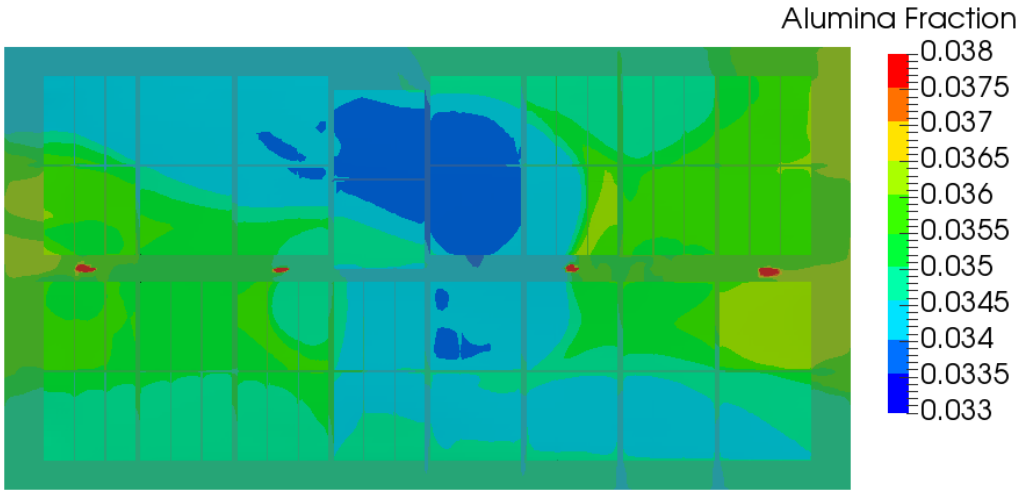

Figure 10. Alumina concentration in the bath volume after anode A1 is changed, Case 2.

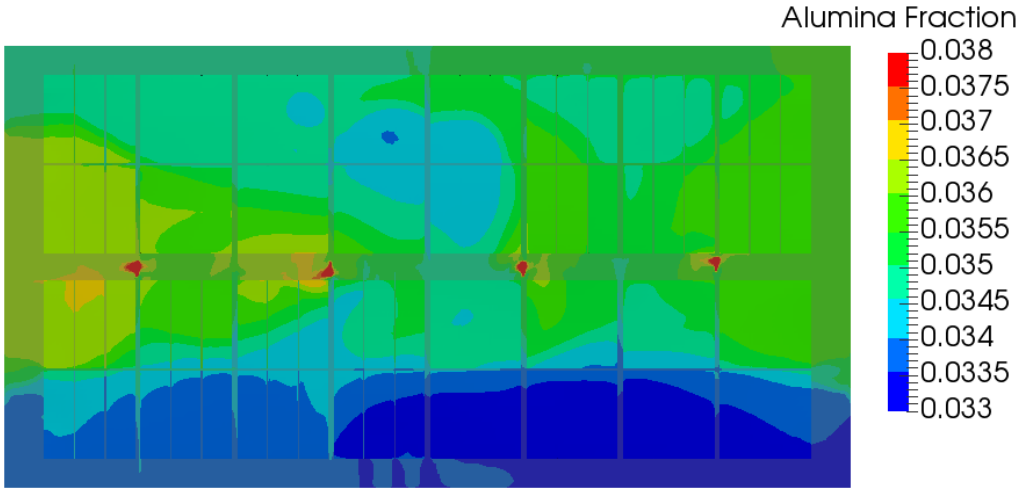

Figure 11. Alumina concentration in the bath volume after anode A1 is changed, Case 3.

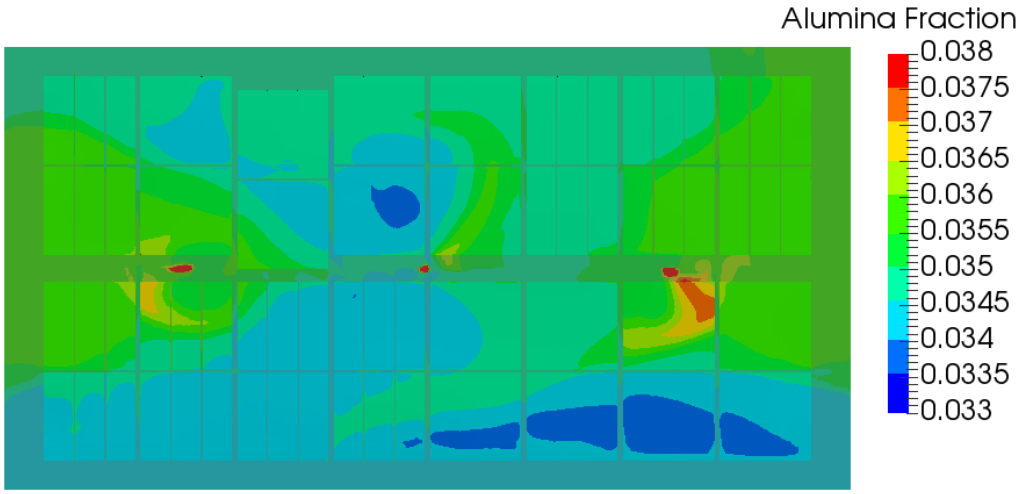

Figure 12. Alumina concentration in the bath volume after anode A1 is changed, Case 4.

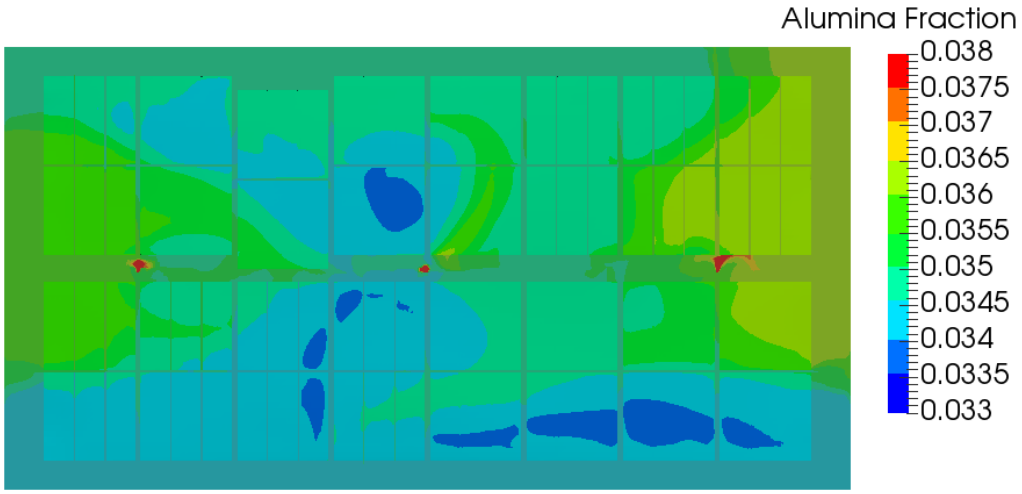

Figure 13. Alumina concentration in the bath volume after anode A1 is changed, Case 5.

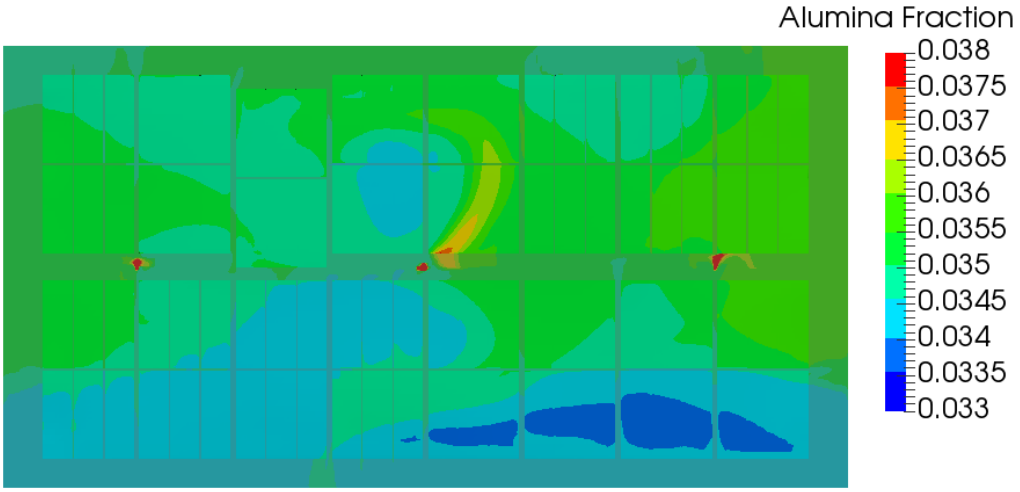

Figure 14. Alumina concentration in the bath volume after anode A1 is changed, Case 6.

6.2 Statistical Comparisons of the Results

In face of the massive amount of produced data, it is necessary to organize and define objective parameters for the comparison and analysis of different cases. Because good alumina concentration homogeneity under the anodes is desired, it has been decided to compute the average alumina concentration under each anode (32 anodes), for each slot configuration (16 anode changes) referent to each anode change (from T1 to T16). These numbers can be summed up and arranged in a histogram of alumina concentration levels.

The Figure 15 presents the alumina concentration under the anode shadow cumulative histogram for each case. It can be visually observed that Case 6 presents lower dispersion. High dispersion can be seen in Case 1 followed by Case 3.

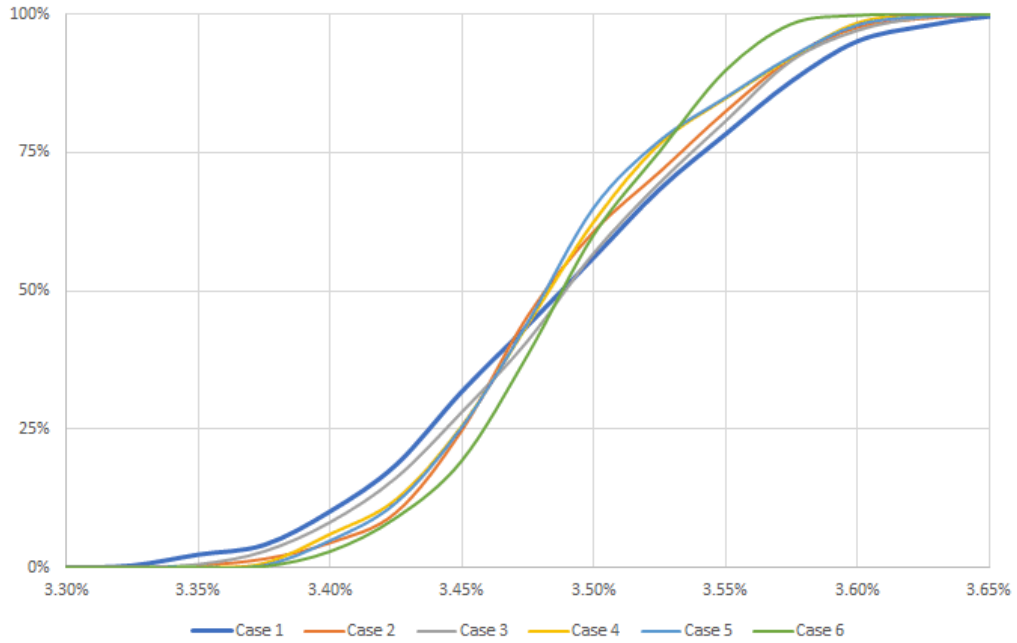

Figure 15. Cumulative histogram of average alumina concentration under each anode for all cases.

The measure of histogram data dispersion is the standard deviation where we can compare all case results, using a single parameter. The Figure 16 show the standard deviation obtained for each case.

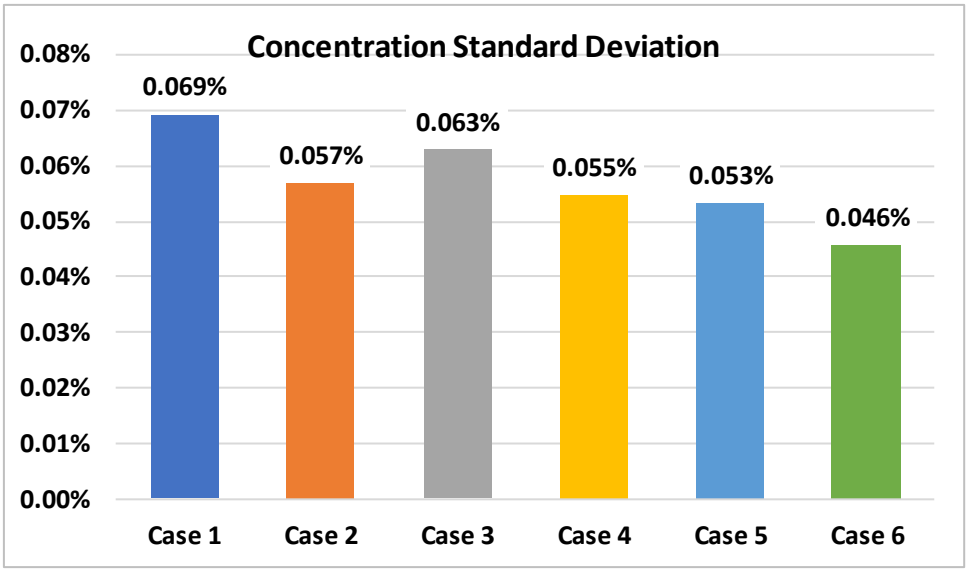

Figure 16. Standard deviation of alumina concentration under each anode, all cases.

The values confirm what has been observed in the histograms. Case 6 presents the best alumina distribution homogeneity while the worst results are observed in Case 1 (actual feeders configuration) followed by Case 3.

Good results were obtained with the A3 tapping channel. One explanation might be because the A3 tapping channel causes a center channel strangulation that is placed between two adjacent feeders (differently from A4 tapping channel), separating the alumina flow of each feeder to different regions instead of directing both to the same location.

In the cases with three feeders, even though the bath height is lower at cell center (because of metal heave), the feeding rate of the middle feeder must be higher (Case 6 against Case 5), because the center feeder is responsible to supply alumina for a large region of the cell.

7. Advective Energy Transport inside the Bath

The objective of this particular model was to study the fate of the energy generated inside the ACD space. It is probable that superheat is going to be higher at the locations where the ACD bath (where the Joule heat is produced) is transported to. In this case, the bath temperature is higher in steady state at a particular region in space due to the continuous heat generation and transport, as distinct from the transient temperature jump caused by an alumina shot.

In order to track such energy, it was possible to adapt the alumina transport models to perform this task. We adopted some assumptions:

- Existing cell tapping configuration was used, anodes without slots;
- Energy distribution was simulated with a scalar transport variable, similar to alumina concentration methodology;
- Advective transport only;
- Energy is generated in all the ACD volume under anode vertical projection;
- Energy leaves the bath at the ledge surfaces and it is also consumed to heat up fresh alumina entering at feeder positions;

This methodology also does not consider heat losses redistribution due to ledge position, the results and conclusions must be interpreted carefully, understanding the model limitations listed

above. The Figure 17 shows the temperature field obtained in the model, above or below the bath bulk temperature.

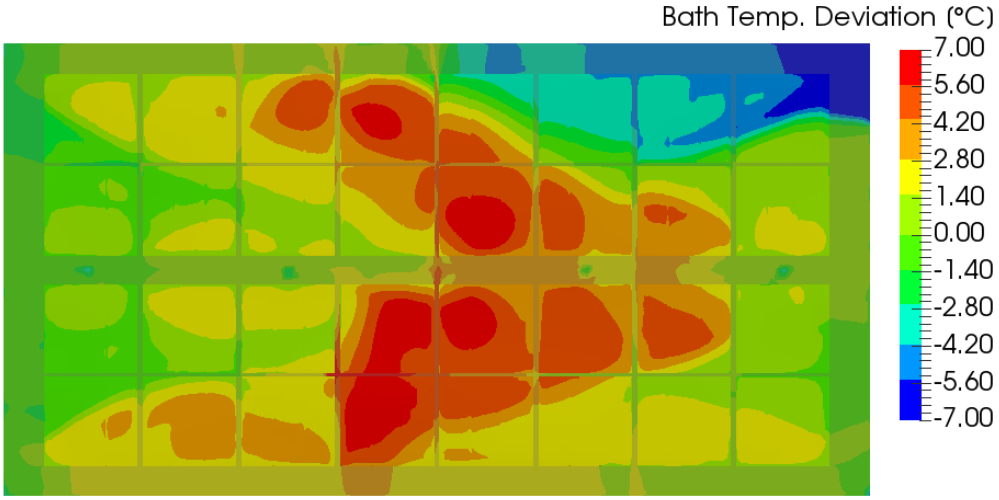

Figure 17. Temperature deviation inside the bath referred to the bath averaged bulk temperature.

The result showed that energy is directed from the ACD to the cell center by the bath flow. It is likely that superheat is higher at the cell center. This might explain the reported observations done by ALUAR staff of bigger flames at the center holes, see Figure 18. There are other possible causes for the flame observations not related with bath transport: burning of carbon dust, burning of CO to CO_2 and gas circulation pattern between the bath surface and the crust.

The result of this chapter supports the idea that feeding the cell at the center promotes better alumina dissolution due to higher superheat, thus reducing the risk of creating sludge.

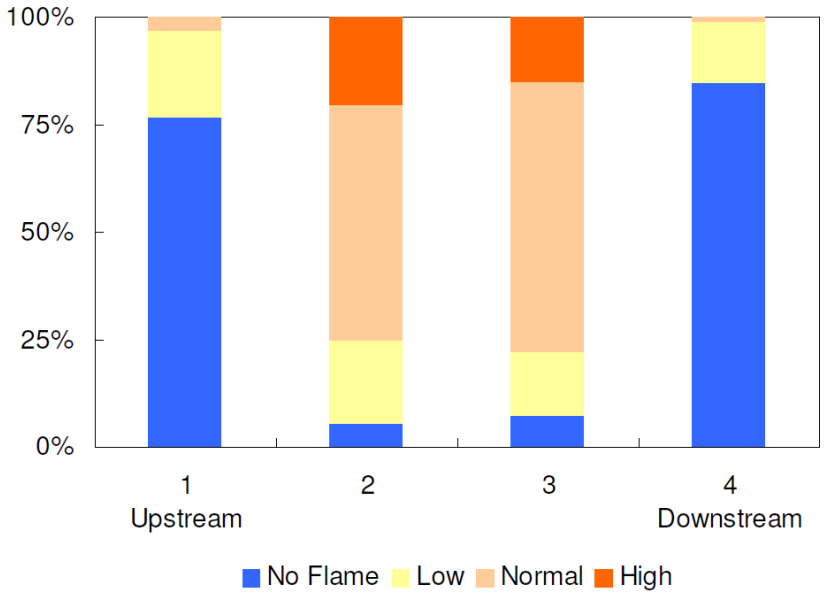

Figure 18. Flame intensity observed at the feeder holes (F1, F2, F3 and F4).

8. Study of Bath Flow Driving Forces

The objective of this study was to understand the importance of each driving force on the final bath flow pattern obtained for the electrolysis cell. The fluid flow inside the bath is originated by the interaction of the following mechanisms:

- Bubble induced forces;
- Volumetric MHD forces inside the bath;
- Metal drag forces (MHD) at bath/metal interface.

In the CFD models, each effect can be separately analyzed by applying only 1 effect at once. The no slot geometry was selected for comparisons, 5 cases were calculated:

1) Real operation, all effects included;
2) Bubble induced only;
3) Metal/bath interface drag forces only;
4) Volumetric MHD forces inside the bath only;
5) Metal/bath interface drag forces + MHD forces inside the bath.

The following pictures (from Figure 19 to Figure 23) present the bath flow calculated for each of above described situations.

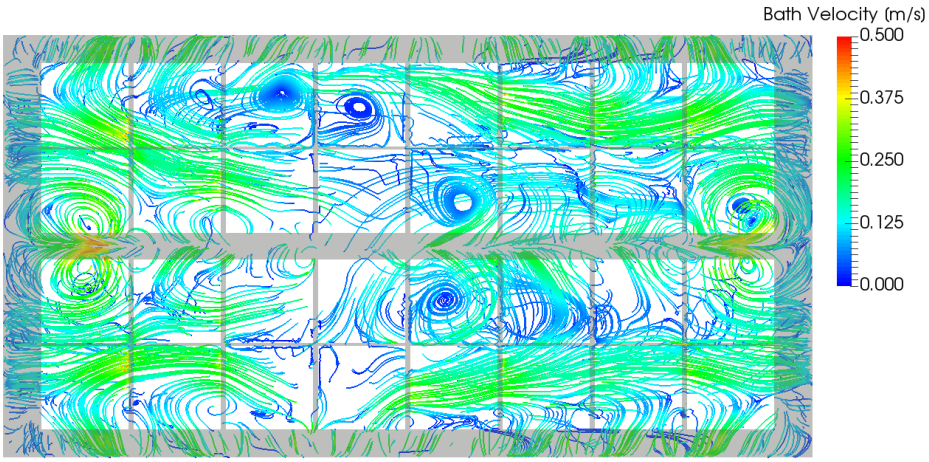

Figure 19. Bath velocities obtained with all forces included.

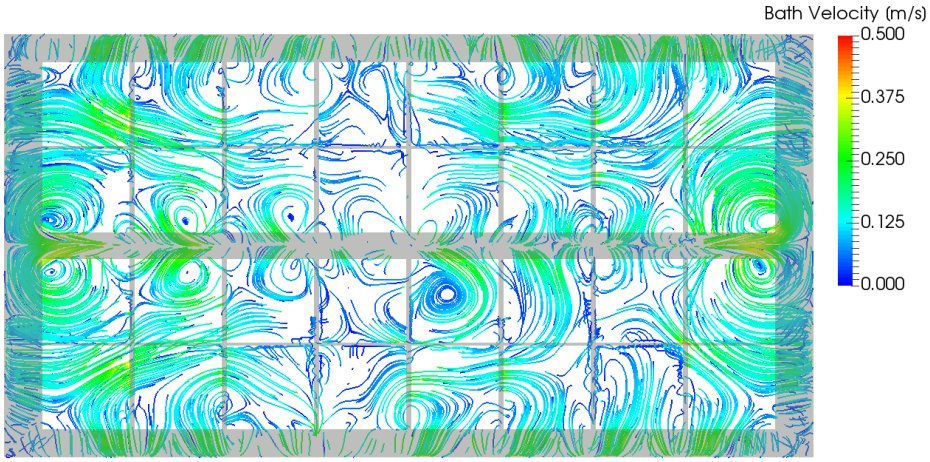

Figure 20. Bath velocities obtained with bubble induced forces.

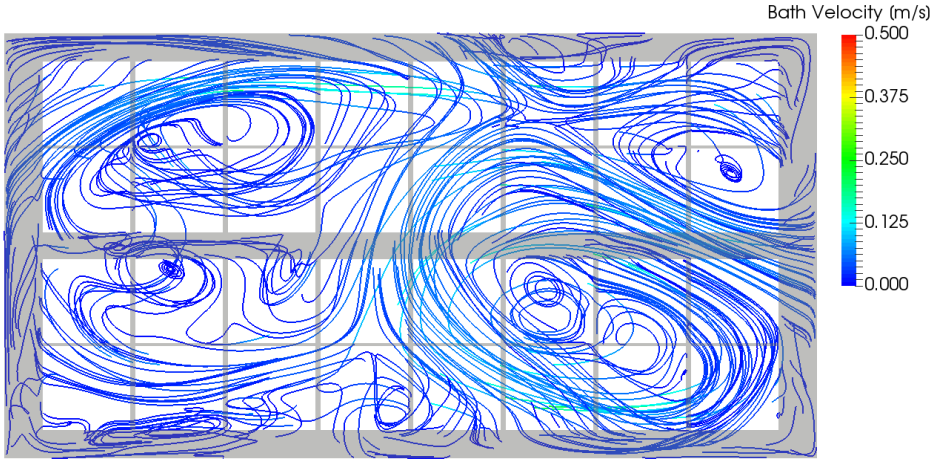

Figure 21. Bath velocities obtained with metal-bath interface forces.

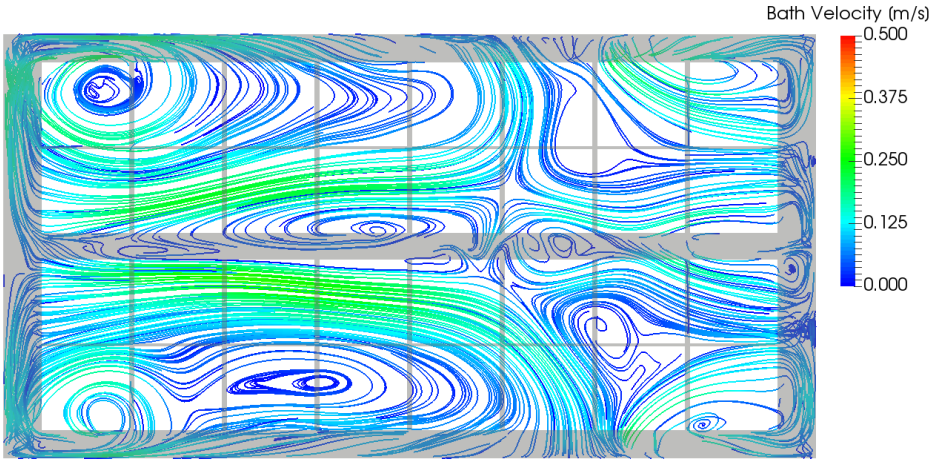

Figure 22. Bath velocities obtained with volumetric MHD forces.

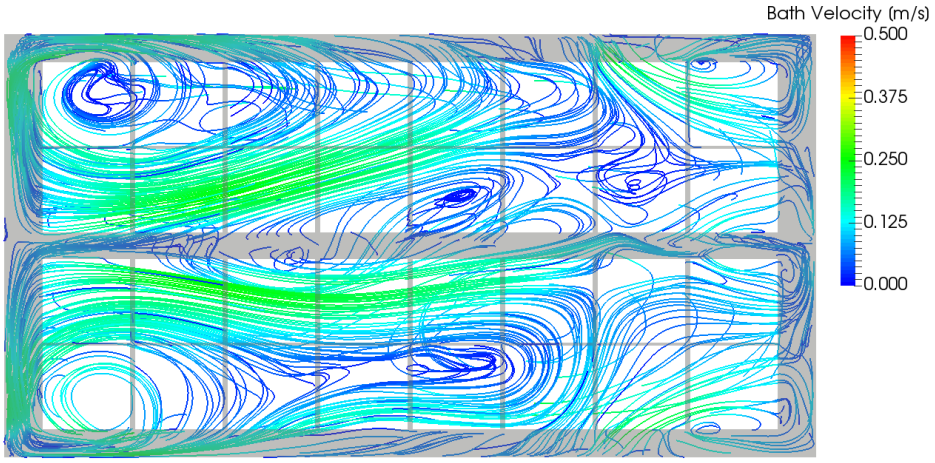

Figure 23. Bath velocities obtained with volumetric MHD forces plus metal-bath interface forces.

By observing the results, it is clear that the flow velocities are dominated by the bubble induced forces. The secondary influence is the MHD volumetric forces and the weakest influence is the metal-bath interface drag forces. However, the MHD forces are responsible to control the large

eddies that communicate the distinct cell regions. Alumina distribution is then strongly influenced by MHD forces.

9. Conclusions

The model for alumina transport inside the bath was successful developed. It presents very good agreement with the bath temperature measurements performed by ALUAR, at least in the cases where the temperature variation was detected at the measurements. It is important to include the bubble induced forces as well as the MHD forces and metal drag in the simulations. The same model can be modified in order to predict the regions of higher bath temperature and superheat. The place and number of feeders can be optimized using the models.

In the particular cell technology presented in this article, if the tapping channel at sidewall is used displacing one anode towards the center channel, the bath flow will be affected, because the center channel must be narrowed. The channel strangulation will improve the alumina mixing, mainly in the A3 tapping channel position. As a consequence, fresh alumina is more homogeneously spread in the bath volume. Usually the central channel is simply focused on sufficient width to distribute alumina, but more complex geometries may improve bath flow pattern helping the alumina distribution.

Analyzing the dispersion found in alumina concentration under the anodes regarding each feeding setup case, we observe that the best alumina distribution was found in Case 6, which uses the A3 tapping channel in combination with 3 feeders. If, for other technical reasons, there is the need to keep using 4 feeders, a good option is case 2 where the tapping position requires displacement of anode A4.

It has been shown in the model that energy generated in the ACD tends to concentrate in the middle of the cell bath layer. In the model, the bath temperature is lower at the feeders near the cell ends. Less flames are observed at these feeder holes in real cells, which may be correlated with the energy transport. The models help to optimize the position of the feeder regarding bath temperature and alumina transport pattern.

10. References

1. Dagoberto S. Severo, Vanderlei Gusberti, Elton C.V. Pinto and Ronaldo R. Moura, Modelling the bubble driven flow in the electrolyte as a tool for slotted anode design improvement, *Light Metals 2007*, 287-292.
2. Rene von Kaenel, Jacques Antille, Michel V. Romerio, Olivier Besson, Impact of magnetohydrodynamic and bubbles driving forces on the alumina concentration in the bath of a Hall-Heroult cell, *Light Metals 2013*, 585-590.
3. Benoit Bardet et al., Alumina dissolution modeling in aluminium electrolysis cell considering MHD driving convection and thermal impact, *Light Metals 2016*, 313-319.
4. Steeve Renaudier, Steve Langlois, Benoit Bardet, Marco Picasso, and Alexandre Masserey, Alucell: A unique suite of models to optimize pot design and performance, *Light Metals 2018*, 541-549.
5. Yuqing Feng, Mark A. Cooksey and M. Philip Schwarz, CFD modelling of alumina mixing in aluminium reduction cells, *Light Metals 2010*, 455-460.
6. Yuqing Feng, Mark A. Cooksey and M. Philip Schwarz, CFD modelling of alumina mixing in aluminium reduction cells, *Light Metals 2011*, 543-548.
7. Jayson Tessier, Katie Cantin, and David Thor Magnusson, Investigation of alumina concentration gradients within Hall-Héroult electrolytic bath, *Light Metals 2018*, 515-522.